Effect of electrolyte composition on rock salt surface degradation in NMC cathodes during high-voltage potentiostatic holds

Adam Tornheim,[a] Soroosh Sharifi-Asl,[b] Juan C. Garcia,[a] Javier Bareño,[a,1] Hakim Iddir,[a] Reza Shahbazian-Yassar,[b] Zhengcheng Zhang[a,*]

[a] Chemical Sciences and Engineering Division
Argonne National Laboratory
9700 S. Cass Ave., Lemont, IL 60439 USA

[b] University of Illinois at Chicago
Department of Mechanical & Industrial Engineering (MC 251)
842 W. Taylor Street, Room 2039 ERF
Chicago, IL 60607-7022 USA

[1] Present address: MIMSI Materials, Teknikringen 7, 583 30 Linköping, Sweden

[*] Corresponding author at: Chemical Sciences and Engineering Division, Argonne National Laboratory, 9700 S. Cass Ave., Lemont, IL 60439 USA
Email addresses: zzhang@anl.gov

Abstract

Surface degradation of lithium-ion cathodes at high voltages represents a significant barrier to increasing the useable energy of conventional cathodes. Though much work has been focused on mitigating the detrimental effects of such phenomena, the complex and correlated mechanisms involved have made progress difficult. Herein, the effect of electrolyte identity on surface degradation is examined. $LiNi_{0.5}Mn_{0.3}Co_{0.2}O_2$ (NMC532)/$Li_4Ti_5O_{12}$ (LTO) full cells were constructed using three different electrolytes: a baseline organic carbonate electrolyte, a baseline organic carbonate electrolyte with an oxidizable additive, and a fluorinated carbonate electrolyte. Each system was subjected to a 60 hour potentiostatic hold at 3.05 V (4.6 V vs. Li^+/Li) and subsequently deconstructed for characterization via transmission

electron microscopy (TEM) and electron energy loss spectroscopy (EELS). Molecular simulations were carried out on each distinct component of the three electrolytes in contact with crystal surfaces of an NMC532 particle. Results indicate an affinity for the additive-containing electrolyte to extract atomic oxygen from the cathode surface, whereas the fluorinated electrolyte components have negligible interactions. Hydrogen abstraction from the baseline electrolyte is facilitated by the NMC532 surface. TEM analysis of cathode surfaces, after the potentiostatic holds, revealed that the NMC532 particles cycled with the additive-containing electrolyte underwent significant surface degradation, including changes to local crystal structure in a region penetrating 20-40 nm from the surface; consistent with oxygen and lithium loss from the cathode material. However, the NMC532 in contact with the fluorinated electrolyte showed a disordered layer of just a few nm in thickness, similar to the depth of crystal disorder observed in pristine NMC532 primary particles. EELS data of the oxygen K-edge also indicated transition metal (TM) reduction, consistent with oxygen loss and changes in crystal structure extending into the cathode surface for each of the electrolytes surveyed. These surface reactions, including oxygen loss, are shown to correlate well with elevated oxidation currents and surface reconstructions of cathode particles.

1. Introduction

Layered transition metal oxides of the molecular formula $LiMO_2$ have received significant interest as cathode materials for lithium-ion batteries due to their high theoretical capacity of ~280 mAh/g.[1] One of the first cathodes in this family, $LiCoO_2$, has seen substantial deployment. However, phase transformations, including spinel formation and accompanying oxygen evolution, at high states of charge can lead to reactions with the electrolyte and thermal runaway,[2] limiting the practical capacity of pure $LiCoO_2$ to about half the theoretical value. Incorporation of other transition metals (Ni, Mn) into the Co sites of the layered lattice (yielding $LiNi_{1-x-y}Mn_xCo_yO_2$, referred to as NMC compounds) preserves the layered ($R\bar{3}m$) structure of $LiCoO_2$ to higher states of charge, partly by suppressing the hexagonal to monoclinic transition at ~$Li_{0.5}CoO_2$, thereby providing benefits over pure $LiCoO_2$ or $LiNiO_2$.[3]

However, thermodynamic simulations indicate that while the pristine, fully lithiated cathode is stable, any amount of delithiation renders the layered $LiCoO_2$ structure unstable against decomposition into $LiCo_2O_4$ and Co_3O_4 spinels.[4, 5] While this decomposition reaction is kinetically hindered in the bulk of the material, facile oxygen loss near the surface of the particles enables local structure changes; especially at high states of charge.[6, 7]

Achieving high capacities with the single-phase $LiMO_2$ cathode materials requires charging to high voltages (>4.5 V vs. Li^+/Li).[8] At this point, in addition to the aforementioned structural instability of the $LiMO_2$, the anodic stability of the electrolyte can also present an issue.[9, 10] Addressing electrolyte instability falls under two broad mechanisms: increasing the intrinsic high-voltage stability of the electrolyte, or, adding sacrificial components/additives to the electrolyte to form a passivating layer on the surface of the cathode.[11, 12] To increase high-voltage stability, the addition of electron-withdrawing groups to the solvent molecules will lower the highest occupied molecular orbital (HOMO) level and result in a molecule that is more difficult to oxidize electrochemically.[13] Using this strategy, fluorinated solvents have been shown to have higher stability to oxidation, and result in better performance with some high-voltage cathodes.[13-18]

Other researchers have reported cathode surface-degradation using atomic-scale characterization techniques and have shown a broad correlation between surface degradation and both applied voltage and temperature during electrochemical testing.[19-22] Additionally, the surface degradation is thought to be a contributor to performance fade.[21, 23] However, much less research has been conducted to elucidate the influence of specific electrolytes in this process, specifically, is there an electrochemical signal of the oxygen loss process, and does the affinity of the electrolyte for oxygen change the amount of oxygen loss and surface degradation under high-voltage conditions.

In this work, we use three electrolytes to span the stability range of both chemical and electrochemical oxidation according to molecular simulations. Tris(2,2,2-trifluoroethyl) phosphite (TTFP), as an additive, has previously been shown to oxidize before baseline electrolytes with inert electrodes as well as significantly increase the oxidation current compared to baseline electrolytes in NMC/LTO full cells.[24, 25] Fluorinated electrolytes have been shown to have much higher electrochemical stability compared to the baseline electrolytes with a variety of cathode chemistries at high voltages. High-voltage potentiostatic holds are typically used to subject the cathode/electrolyte interface to prolonged oxidizing conditions. Herein, we report the effect of electrolyte chemistry/oxidative stability on the surface degradation of charged NMC532 cathode using electron spectroscopy and microscopy (EELS/TEM) and provide a rationale for the surface activity of the various electrolytes on the cathode surface using molecular simulations.

2. Material and methods

2.1 Electrode Materials

The weight composition of the positive electrode used in these experiments was 90% $Li_{1.03}(Ni_{0.5}Mn_{0.3}Co_{0.2})_{0.97}O_2$ (Toda Kogyo Corp.), 5% C45 conductive carbon (Timcal), and 5% PVdF (Solvay 5130) by weight. The positive electrode material was coated on a 20 μm Al current collector to a gravimetric loading of 4.08 mg/cm^2. The weight composition of the negative electrode was 87% $Li_4Ti_5O_{12}$ (NEI), 5% C45 conductive carbon (Timcal), and 5% PVdF binder (Kureha 9300). The negative electrode material was coated on a 20 μm Al current collector to a gravimetric loading of 26.07 mg/cm^2. Neither electrode was calendered, leading to a porosity of ~50%. Electrodes were heated at 70°C in a vacuum oven before being transferred to an air- and moisture-free glovebox (MBraun).

2.2 Electrolytes and Additives

The three electrolytes used in this study were 1) a baseline electrolyte consisting of 1.2 M $LiPF_6$ in a 3:7 w/w mixture of ethyl carbonate (EC) and ethyl methyl carbonate (EMC) (Tomiyama), referred to as Gen2; 2) the baseline electrolyte with 10 wt.%

tris(2,2,2-trifluoroethyl) phosphite (TTFP), an additive that has been shown to lead to higher oxidation currents with high voltage cathodes; and 3) a high voltage fluorinated electrolyte referred to as FE-3, comprising 1 M $LiPF_6$ in 3:7 w/w mixture of trans-4,5-difluoro-1,3-dioxolan-2-one or difluoroethylene carbonate (DFEC) and bis(2,2,2-trifluoroethyl) carbonate (HFDEC).

2.3 Electrochemical Testing Protocol

Cells were assembled in a 2032 coin-cell format with ⌀14 mm electrodes, ⌀16 mm PP/PE/PP separators (Celgard), and 56 µL of electrolyte (roughly 3x the total pore volume of the electrode stack). After assembly, the cells were rested at room temperature for 2 hours before electrochemical cycling to allow for electrode wetting. The cycling protocol comprises a single 150 µA cycle (~27 mA/g_{oxide}) followed by ten cycles at 500 µA (~85 mA/g_{oxide}). These initial cycles were between 2.85 V and 1.45 V (4.4 to 3.0 V vs. Li^+/Li). The cells were then charged at 150 µA to 3.05 V (4.6 V vs. Li^+/Li) and held at that potential for 60 hours. After the 60 hours had elapsed, the cells were discharged to 1.45 V. This protocol is shown in Figure 1.

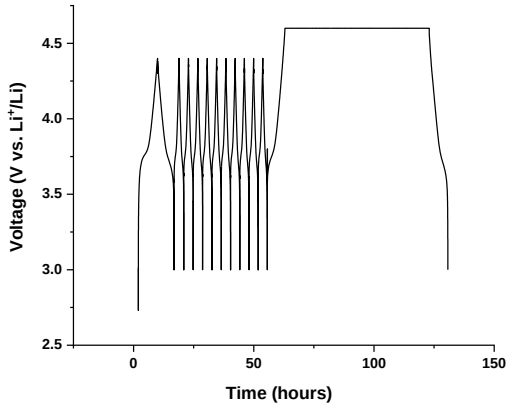

Figure 1. Voltage applied to the cathode (vs. Li^+/Li) as a function of time during the electrochemical protocol conducted before cell disassembly. Note that the LTO anode employed causes the measured cell voltage to be 1.55 V lower than depicted in the figure.

2.4 Electron Microscopy

The coin cells were disassembled in a glove box after the electrochemical cycling. The cathode laminates were submerged into dimethylcarbonate (DMC) for 1 hour then rinsed with fresh DMC three times and dried under vacuum overnight. The laminates were then scraped to obtain cathode powders. The obtained powders were dispersed in methanol and sonicated, drop casted onto a lacy carbon grid, and loaded into the microscope with minimum exposure to air.

Atomic resolution high-angle annular dark-field (HAADF) imaging and EELS were performed using JEOL JEM-ARM200CF STEM. This microscope is equipped with a cold field emission gun and a spherical-aberration corrector that allows for 0.78 Å spatial resolution. A 22 mrad probe convergence angle was used to perform STEM imaging. A HAADF detector with 90 mrad inner-detector angle was utilized to obtain Z-contrast atomic resolution images. EELS was carried out by a Gatan Enfina detector, using 0.3 eV/channel dispersion and a 2 mm detector aperture. The full-width half maximum of the zero-loss peak was measured to be 0.9 eV that determines the energy resolution of the obtained spectra. EELS spectrum imaging was carried out using a 35 pA electron beam, 0.2 s/pixel dwell time and pixel size of 1-2.5 nm in different experiments. Then, the pixels of spectrum image are summed together to reconstruct single spectrums as a function of distance from the surface. Such spectrums are presented in the form of line scans in the paper. The $O_{\text{k-edge}}$ is analyzed to identify the transition metal valence reduction as a function of distance from the surface in different samples. Some HAADF images have been filtered using a HRTEM filter. Fast Fourier transform (FFT) analysis has been conducted on some of the HAADF micrographs using the Digital Micrograph package. Structure distribution maps are produced from some micrographs as follows. For each phase (crystal structure) of interest, characteristic spots are selected and an inverse FFT is applied while masking other contributions to the original FFT. Then, the set of single phase (crystal structure) distribution maps is combined into a false color image.

2.5 Molecular Simulations

All calculations were carried out by spin-polarized density functional theory (DFT) as implemented in the Vienna Ab Initio Simulation Package (VASP).[26, 27] The exchange-correlation potentials are treated by the generalized gradient approximation (GGA) parametrized by Perdew, Burke, and Ernzerholf (PBE).[28] The interaction between valence electrons and ion cores is described by the projected augmented wave (PAW) method.[29] Furthermore, the GGA+U scheme is used for applying the on-site correlation effects among 3d electrons of the TMs, where the parameter of (U-J) is set to 5.96 eV, 5.00 eV, and 4.84 eV for Ni, Co, and Mn respectively.[30] The wave functions were expanded in the plane wave basis up to a kinetic energy of 500 eV. Ionic positions were relaxed to a convergence level of $\Delta E \leq 0.003$ eV. After geometry optimization within the DFT+U framework, a single point energy calculation was performed with the hybrid functional HSE06.[31] Adsorption and reaction energies (ΔE) were calculated using the following expression:

$$\Delta E = E_{surf+adsorbate} - E_{surf} - E_{adsorbate} \quad (1)$$

In Eq. 1, $E_{adsorbate}$ is the energy of the isolated molecule in the vacuum, E_{surf} is the energy of the bare cathode slab, and $E_{surf+adsorbate}$ is the total energy of the molecule adsorbed on the slab. Bulk solvent effects were accounted for by using an implicit solvation model as implemented in VASP.[32, 33] Additionally, calculations of reaction in solution were performed with the Gaussian 09 implementation of DFT at the B3LYP/6-31+G(d,p) level of theory.[34] Frequency calculations were performed for all structures in order to determine the nature of the stationary points. The ultrafine integration grid was employed in all calculations.

3. Results

3.1 Surface Simulations

DFT calculations were used to study the interaction of each electrolyte component (The TTFP additive as well as the solvent molecules EC, EMC, DFEC, and HFDEC) with the NMC surface. Based on previous work that determined that the (012) facet is the

most abundant and reactive NMC surface,[35] we used this prototype surface in our calculations. In addition to DFT, we also used *ab initio* molecular dynamics (AIMD) to explore the configuration space of the molecules over the surfaces. We tested several adsorption configurations in order to find atomic positions that minimized the adsorption energy on both the fully lithiated and fully delithiated surface slab models. Some of these configurations are presented in Figure 2.

Figure 2a shows the lowest energy configuration for EMC solvent on a fully lithiated (discharged) NMC (012) surface. In this conformation, the EMC molecule is chemically oxidized via hydrogen abstraction. The calculated reaction free energy is negative, -0.19 eV, indicating an exothermic reaction. This hydrogen abstraction reaction transfers one electron to the NMC lattice, available to reduce a TM atom, and produces a radical that is stable under the simulation conditions. However, this radical intermediate is highly reactive. The reactivity of this radical intermediate is studied by adding an alkene molecule to the simulation box. The results showed that in the presence of an alkene, this radical intermediate initiated the polymerization of the alkene until a termination step is provided.

Similarly, EC solvent interaction with the NMC surface (equilibrium adsorption configuration shown in Figure 2b) follows the same hydrogen abstraction process. The calculated EC oxidation energy on NMC (012) of -0.72 eV is more favorable than EMC**.** Neglecting EC-EMC interactions, this result indicates that EC would decompose preferentially. Upon delithiation, the thermodynamic driving force for hydrogen abstractions is even larger. The calculated oxidation energy on the delithiated slab is -1.96 eV for EC and -0.56 eV for EMC.

In contrast, the fluorinated solvent molecules HFDEC and DFEC do not react readily with the NMC surface. Figures 2c and 2d show their adsorption configurations on the lithiated slab. Both HFDEC and DFEC interact weakly with the surface, as shown by their low adsorption energies of -0.11 eV and -0.03 eV, respectively. Upon delithiation of the slab, the adsorption energy is relatively unchanged for HFDEC (-0.12 eV) and a

little more favorable for DFEC (-0.22). The geometric configuration of the HFDEC and DFEC molecules is the same on both lithiated and delithiated slabs. Additionally, no charge transfer to the NMC surface was detected in any case. Hence, no TM reduction is expected.

On the other hand, the interaction of the TTFP additive with the NMC surface shows a strong dependence on the slab lithiation state. TTFP interacts weakly (ΔE=-0.04 eV) with the fully lithiated NMC surface, comparable to fluorinated solvent molecules. In contrast, TTFP binds to the delithiated NMC surface much more strongly (-3.1 eV). TTFP forms a strong phosphorous-oxygen bond with the surface oxygen (see the configuration shown in Figure 2e). Furthermore, our results show that there is no energy barrier for the TTFP molecule to remove the P-bound oxygen from the surface and detach as a tris(2,2,2-trifluoroethyl) phosphate (TTFPa) molecule, leaving an oxygen vacancy behind (final configuration shown in Figure 2f). Indeed, the calculated reaction energy (ΔE=-3.1 eV) of taking an oxygen from the surface at this level of lithiation is very similar to the computed energy of oxidation of TTFP to TTFPa in solution (ΔE=-3.5 eV); and the formation energy of an oxygen vacancy at the surface of the delithiated NMC is negligible.[35] In addition to being thermodynamically favorable, TTFP oxidation to TTFPa by removal of an O atom from the NMC surface involves the transfer of two electrons to the NMC lattice. This transfer can be expected to reduce the TMs and, in concert with oxygen loss from the surface, stabilize more reduced metal oxide forms like spinel M_3O_4 and rock salt MO. Also, hydrogen abstraction is not observed when TTFP interacts with the surface, probably due to steric hindrance.

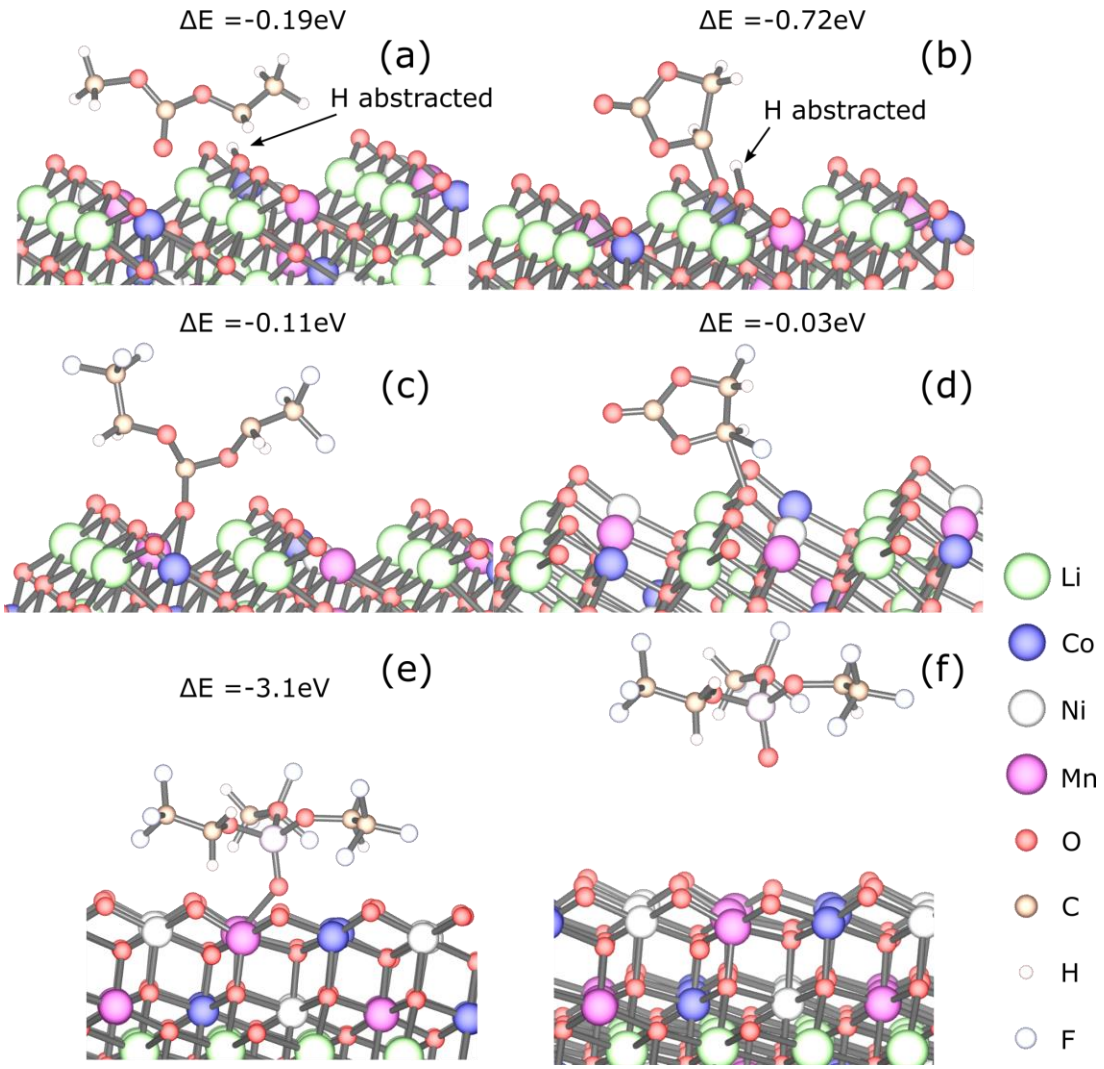

Figure 2. Lowest energy configuration of electrolyte components at or near the (012) facet of (a-d) fully lithiated or (e-f) fully delithiated NMC532. (a) EMC, (b) EC, (c) HFDEC, (d) DFEC, (e) TTFP on delithiated NMC, and (f) TTFPa detached from NMC surface.

3.2 Electrochemical Treatment

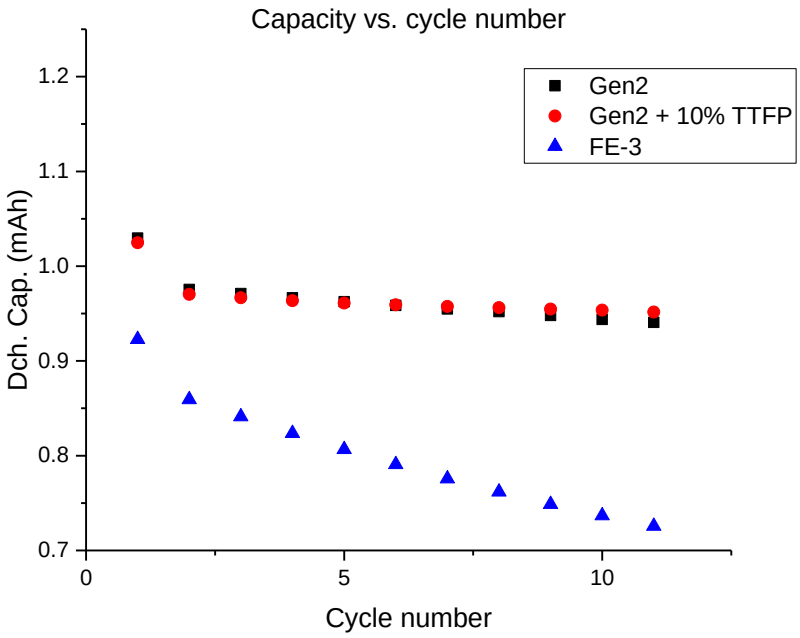

Figure 3. Discharge capacity vs. cycle number for the cycles before the potentiostatic hold. (See protocol in Figure 1 and text for details).

Armed with these insights into the reactivity of different electrolyte components, we set to investigate the NMC response to cycling in three different electrolytes. The baseline case employs Gen2 electrolyte, 1.2 M $LiPF_6$ in a 3:7 w/w mixture of EC and EMC. We compare it to two other electrolyte systems: (1) Gen2 + 10% TTFP, a modification of the Gen2 electrolyte containing 10% wt. of TTFP, an additive that has been shown to lead to higher oxidation currents with high voltage cathodes; and (2) FE-3, an electrolyte comprising $LiPF_6$ with highly fluorinated solvents.

Figure 3 shows the discharge capacity vs. cycle number of NMC/LTO coin cells containing each of these three electrolytes. The cell containing the Gen2+TTFP electrolyte shows similar discharge capacity to the cell containing the baseline Gen2 electrolyte. However, the cell containing the fluorinated FE-3 electrolyte shows lower initial capacity and worse capacity retention. This is likely due to the cathodic instability of the FE-3 electrolyte on the LTO electrode, which causes Li trapping and,

subsequently, loss of cycleable lithium. However, as the LTO is a phase change anode with a constant voltage,[36] this lithium trapping would not affect the potential applied to the cathode during the potentiostatic hold. In this way, all three cathodes were exposed to the same abusive conditions during the high-voltage hold.

3.2.1 Potentiostatic Hold Current

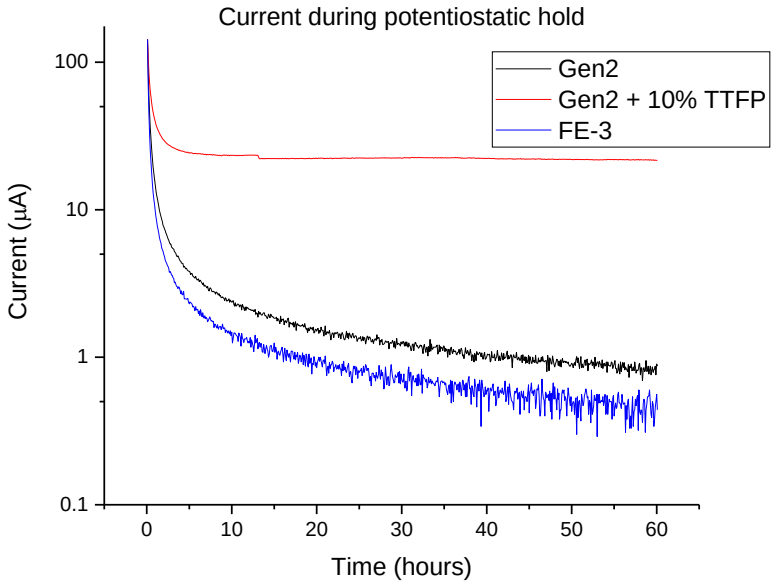

Figure 4. Current as a function of time for the three electrolytes during the 4.6 V vs. Li^+/Li potentiostatic hold.

After the eleventh cycle, the cells were charged at 150 μA to 3.05 V (cathode voltage is 4.6 V vs. Li^+/Li), and held at that potential for 60 hours. Figure 4 shows the oxidation current during the potentiostatic hold for the three electrolytes. Upon reaching the voltage of the potentiostatic hold, the current decays quickly as the concentration polarizations relax, and at this point, side-reaction currents become more evident. The baseline electrolyte with the TTFP additive shows the highest current, approximately 22 μA at steady state. This oxidation current is significantly

larger than for the Gen2 and FE-3 electrolytes, 0.84 μA and 0.46 μA, respectively. The total charge passed follows the same relation.

3.3 STEM-EELS analysis of NMC532

After completing the electrochemical protocol described above, the cells were disassembled in the glovebox and prepared for TEM analysis. In the following paragraphs and figures (Figures 5 to 8), we present micrographic (HAADF-STEM) and spectroscopic (EELS) evidence of the migration of TM atoms within the fcc oxygen lattice of the NMC cathode in response to the loss of Li (due to cathode oxidation) and O (due to reactions with the electrolyte). Figures 5, 6, and 7 present HAADF-STEM images and STEM-EELS line scans of the near-surface regions of NMC particles cycled in the different electrolytes. Figure 5 is from NMC cycled in Gen2 electrolyte containing 10% TTFP, Figure 6 from NMC cycled in Gen2 electrolyte without TTFP (baseline), and Figure 7 from NMC cycled in the fluorinated FE-3 electrolyte. In each figure, HAADF-STEM micrographs show regions with local spinel ($Fd\bar{3}m$) and rock salt ($Fm\bar{3}m$) crystal structures within the layered ($R\bar{3}m$) NMC. When indexing these areas, and for the sake of clarity, we use sub-indexes L, S, or C to indicate directions and planes indexed in the layered, spinel or rock salt basis, respectively.

Looking first at the Gen2+TTFP cycled cathode, Figure 5a shows a low magnification HAADF-STEM image of a cathode particle tested in the Gen2+TTFP electrolyte and imaged along the $[001]_L$ zone axis (Z.A.). Figures 5b and 5c are lattice-resolution HAADF-STEM micrographs of the two highlighted regions in Figure 5a; 5b near the edge of the particle and 5c further into the bulk. The insets in Figures 5b and 5c are FFT's of the corresponding images.

The area close to the edge of the particle (Figure 5a) shows a speckled contrast, in a region spanning ~50 nm away from the edge and into the bulk (scale bar = 50 nm), that is absent in the bulk of the particle. This contrast is indicative of local changes in density stemming from crystal structure changes, void formation, and or surface damage. The higher magnification image (5 nm scale bar) of the edge region in Figure

4b reveals an irregular, rather than sharp particle edge. The hexagonal arrangement of atomic columns, with intercolumnar spacing of 15 nm, is difficult to resolve, although some areas close to the edge show a clear hexagonal atomic arrangement with twice the spacing. The same hexagonal atomic arrangement is clearer in the deeper area shown in Figure 5c (e.g. near the center and top-center areas of the image, 5nm scale bar). Correspondingly, a double-spaced hexagonal arrangement of bright columns is also evident in some areas of Figure 5c. (e.g., at the middle of the left side of the figure).

The FFT's of these images (insets in Figures 5b and 5c) contain twelve spots at the vertices of two concentric hexagons. The outer hexagon in each FFT can be indexed either as the $\{20\bar{2}\}_C$ spots expected in the $[111]_C$ Z.A., the $\{1\bar{2}0\}_L$ spots of the $[001]_L$ Z.A., or the $\{40\bar{4}\}_S$ spots of the $[111]_S$ Z.A. The spots in the inner hexagon can only be indexed as the $\{20\bar{2}\}_S$ spots of the spinel structure; or ½ spinel super reflections on the L or C (rock salt) parent structures. The outer hexagon spots arise from the overall hexagonal arrangement of atomic columns described above. Conversely, the inner hexagon spots arise from the double-spaced hexagonal arrangement of columns visible in some areas of Figure 5c. The inner hexagon of spots is not as clear in the FFT of Figure 5b as it is in Figure 5c and, correspondingly, the double-spaced hexagonal arrangements of columns are not as prominent as in Figure 5c.

Due to the lack of characteristic periodicities (spots in FFT), this projection cannot be used to distinguish between the layered and rock salt structures. However, the presence of spinel-reconstructed domains is evident, both close to the surface of the particle (Figure 5b) and further into the bulk (Figure 5c). Correspondingly, the O-K pre edge (Figure 5d) becomes less pronounced and shifts to higher energy loss at a depth of ~40 nm into the bulk and extending to the surface, consistent with lower transition metal oxidation states.

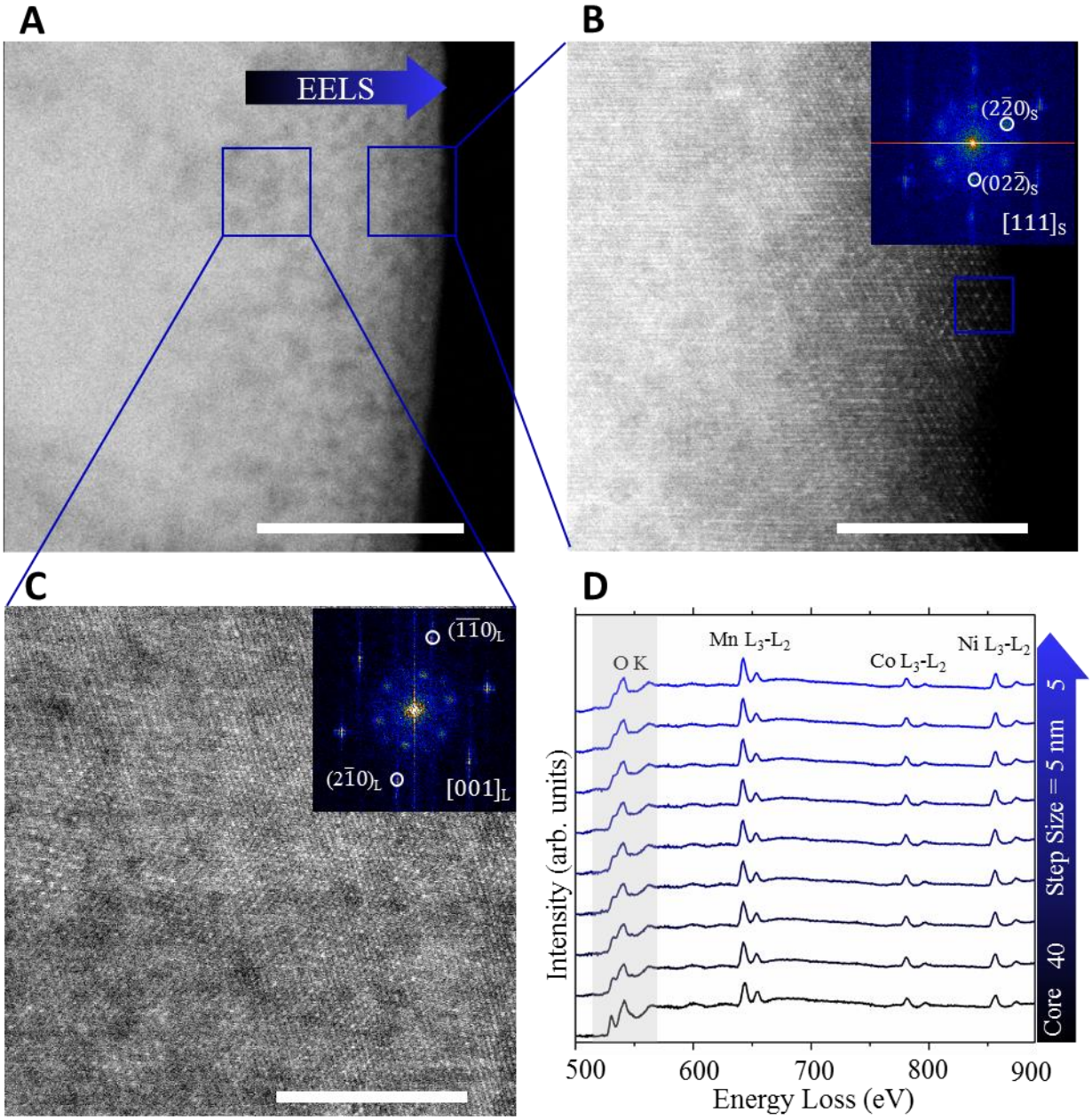

Figure 5. HAADF-STEM micorgraphs (a-c) and EELS scan spectra (d) from an NMC532 particle cycled in Gen2+TTFP electrolyte. (a) Low magnification image of the particle, 50 nm scale bar. (b) Atomic resolution image of the surface region indicated in (a), 5 nm scale bar. (c) Atomic resolution image of a deeper region as indicated in (a), 5 nm scale bar. (d) Spectra from EELS line scan (40 nm range, 5 nm steps) on the area indicated in (a).

Figure 6a shows a low magnification HAADF-STEM image of a cathode particle tested in the baseline Gen2 electrolyte without the TTFP additive. Figure 6b shows a higher magnification image and corresponding FFT (inset) of the area highlighted in Figure 6a, close to the surface of the particle.

The FFT in Figure 6b can be indexed as a $[111]_S$ Z.A. The presence of $\{20\bar{2}\}_S$ spots in this FFT is a clear indication of the presence of areas with local spinel symmetry close to the surface of this NMC particle cycled in Gen2 electrolyte. Additionally, the STEM-EELS spectra presented in Figure 6c display a prominent O-K edge pre-peak in the scans recorded far away from the particle surface. As was the case in Figure 5, this pre-peak shifts to higher energy loss and becomes less pronounced as the EELS probes gets closer to the particle surface. However, the changes in the O-K edge shape clearly extend deeper into the particle cycled in Gen2+TTFP electrolyte (~40 nm, Figure 5d) than in the Gen2 electrolyte (~20 nm, Figure 6c).

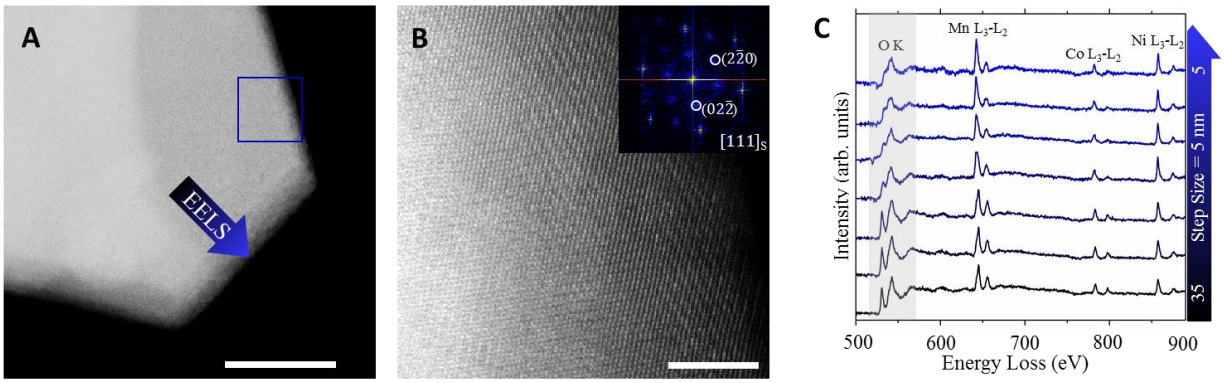

Figure 6. HAADF-STEM micorgraphs (a-c) and EELS scan spectra (d) from an NMC particle cycled in Gen2 electrolyte, without additives. (a) Low magnification image of the particle, 50 nm scale bar. (b) Atomic resolution image of the surface region indicated in (a), 5 nm scale bar. (c) Spectra from EELS line scans (40 nm range, 5 nm steps) on the area indicated in (a).

Figures 7a through 7c show high magnification HAADF-STEM micrographs of cathode particles cycled in the FE-3 electrolyte. Figure 7a shows an area of the particle surface

and Figure 7b an area adjacent to the particle surface, both observed along the $[12\bar{1}]_L$ Z.A. The FFT inset in Figure 7b clearly shows $\{\bar{1}11\}_S$ (or, alternatively, $\frac{1}{2}\{012\}_L$) spinel (super)spots, indicating the presence of regions with local spinel symmetry close to the surface of the particle. At the top-left corner of Figure 7b, a false color section of the micrograph highlights the presence of both layered and spinel regions. Fourier filtering of the original micrograph was used to produce the image. A $\{\bar{1}11\}_S$ spot gives rise to the spatial intensity distribution plotted in blue, while two $\{101\}_L$ spots are used to calculate the gray. The composite image clearly shows separate locations of local, layered and spinel symmetries.

Figure 7c shows a side view, along the $[110]_L$ Z.A., of the surface area of the NMC particle. The bulk regions of the particle clearly show the alternating sequence of TM and Li planes (labeled "Li^+ Transport channels" in the image, because of facile Li diffusion in these planes). An approximately 5 nm thick layer at the surface of the particle, labeled "Cation Disordered Area" in the image, shows atomic column contrast in the Li planes, indicating the presence of migrated TM atoms. This is consistent with both local rock salt and spinel structures. The FFT inset in the top-right corner of the image, calculated from the whole field of view, displays all the features expected from the layered structure with no spinel super-reflections present. On the other hand, the FFT inset on the bottom-right corner of the panel, calculated from the "Cation Disordered Area", lacks any superspots characteristic of either a layered or spinel structure and can be indexed as a $[\bar{1}10]_C$ Z.A. While the lack of spinel reflections could still be attributed to insufficient volume fraction of some spinel-transformed regions to generate appreciable signal in the FFT, it can also be attributed to a thin reconstructed surface layer with an average rock salt symmetry.

Finally, Figure 7d presents the STEM-EELS spectra acquired at different distances from the particle surface. Compared to the corresponding EELS spectra in Figures 5 and 6, the changes to the O-K edge of the sample cycled in the FE-3 electrolyte are smaller and more confined to the surface. This is more easily seen in Figure 8, which

plots the difference in energy, ΔE, between the O-K pre- and main peaks as a function of distance to the surface for the particles cycled in the three electrolytes of interest.

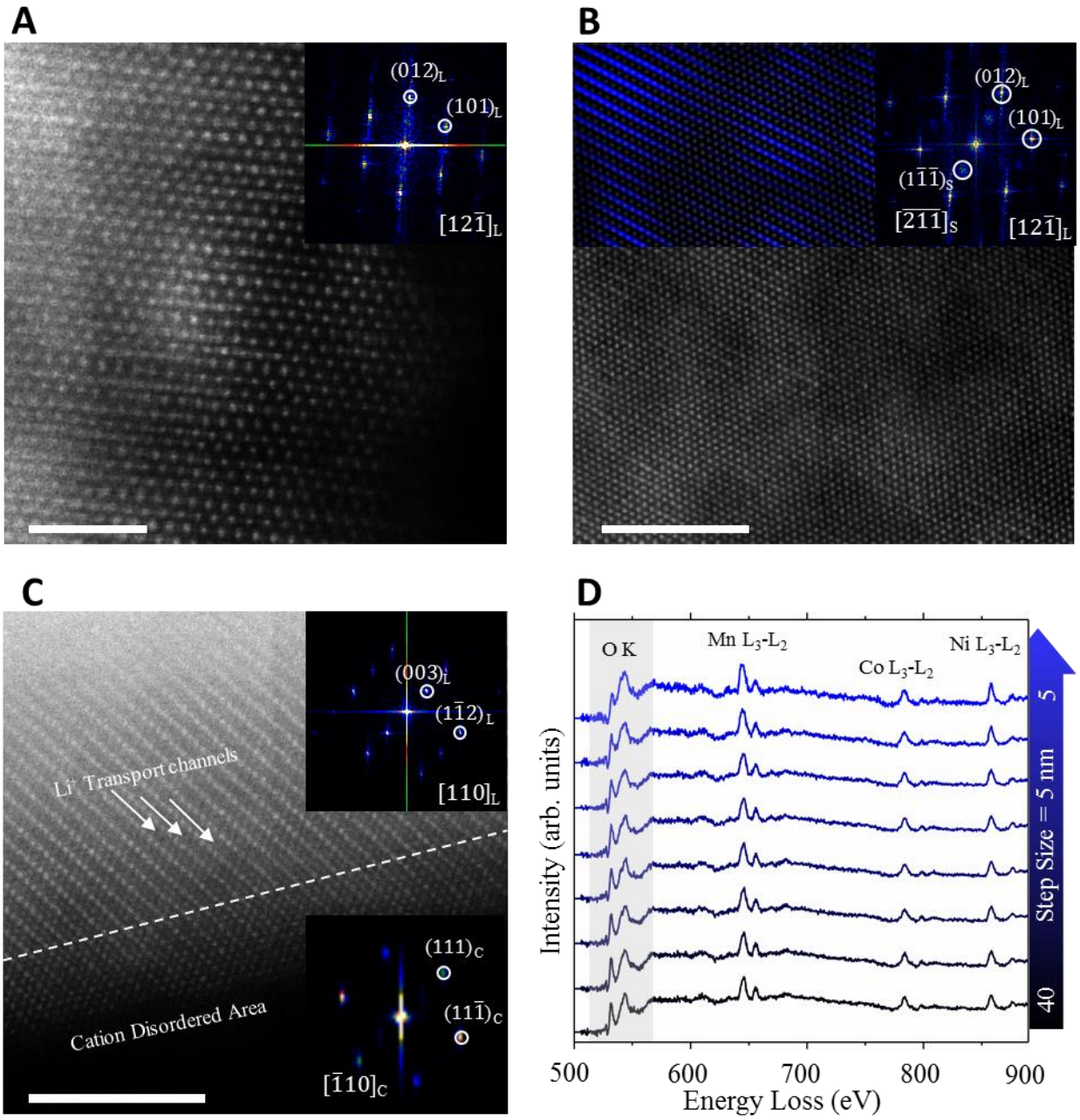

Figure 7. HAADF-STEM micorgraphs (a-c) and EELS scan spectra (d) from NMC particles cycled in FE-3 electrolyte. (a) Atomic resolution image of a surface region, 2 nm scale bar. (b) Atomic resolution image of a region adjacent to the surface, 5 nm

scale bar. (c) Atomic resolution, side view of a surface region, 5 nm scale bar. (d) Spectra from EELS line scans (40 nm range, 5 nm steps) approaching the surface of the particle. See text for inset details.

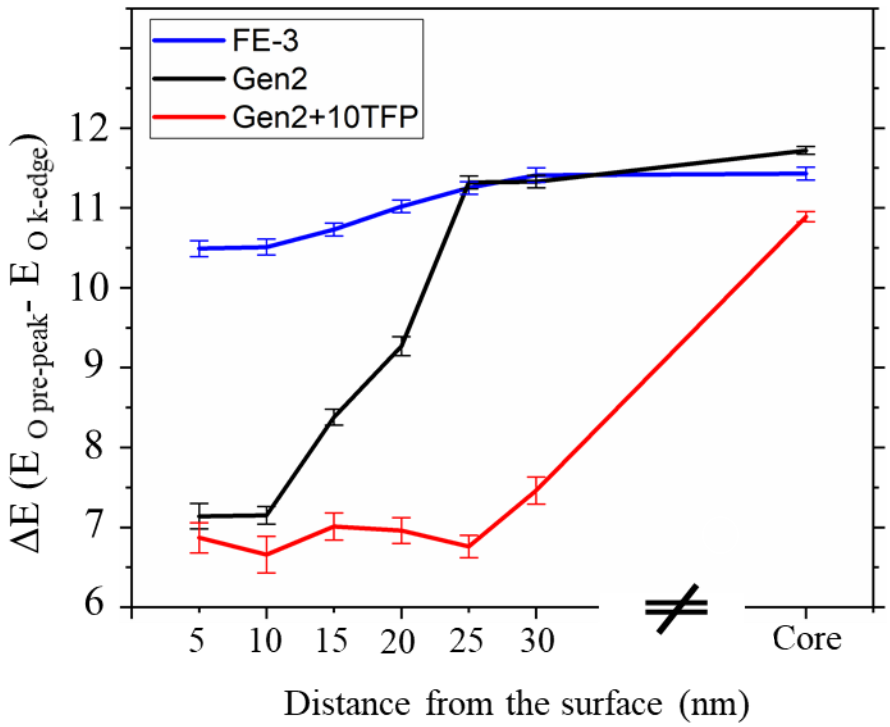

Figure 8. EELS analysis results from NMC samples cycled with various electrolytes. Energy difference between the O-K edge and its pre- peak is plotted as a function of distance from the surface.

In the EELS results shown in Figures 5d, 6d, and 7d, all spectra show O-K, Mn-L, Co-L, and Ni-L edges around 530 eV, 640 eV, 780 eV, and 880 eV, respectively. The O-K edges consist of a pre-peak and a main peak, with the pre-peak appearing at lower energy loss than the main peak. Both pre- and main peaks are due to transitions between O 1s and two kinds of O 2p states; O 2p states hybridized with metal 3d states for the pre-peak and O 2p states hybridized with metal 4sp states for the main peak. Correspondingly, metal L edges show two peaks, L3 and L2, corresponding to transitions from $2p_{3/2}$ and $2p_{1/2}$ metal orbitals, respectively, to metal 3d orbitals.

While all these edges are useful to determine oxidation state of the TMs,[37, 38] we focus our analysis on changes to the O-K edge. In particular, we use the energy difference ΔE between the pre- and main peaks of the O-K edge, determined from fitting a Gaussian to each peak, as an indication of the local oxidation state of the metals.[39] This ΔE is plotted in Figure 8 as a function of distance to the particle surface, for each electrolyte system considered.

The particles cycled in Gen2 and FE-3 electrolytes present values of ΔE ≃ 11.5 eV at the core of the particle (~40 nm). This value is approximately maintained up to a distance of ~25 nm from the surface. At that point, the ΔE value of the Gen2-cycled particle decays rapidly to ≃ 7 eV at a depth of ~10 nm, where it remains up to the particle surface. Conversely, the FE-3 cycled particle decays much less over the same range, decreasing by only ~1eV to ΔE ≃ 10.5 eV. However, the Gen2+TTFP cycled particle starts at a slightly lower ΔE of ≃ 10.5 eV at the core of the particle, which is reduced to ΔE ≃ 7 eV at a depth of 25 nm and remains at this value up to the surface of the particle. As can be seen in Figure 8, this low ΔE region extends deeper into the particles cycled in Gen2 + 10% TTFP electrolyte as compared to the particles cycled in the other two electrolytes.

4. Discussion

For the three electrolytes surveyed, simulations predicted different interaction energies as well as reaction mechanisms with the charged cathode surface. In order to connect these predicted interactions with the observed electrochemistry, we need to understand their contribution to the current signal during the potentiostatic hold experiments. While this technique has been explained more thoroughly in previous work,[40] the relevant takeaways are summarized in the following paragraphs for the reader's convenience.

During a potentiostatic hold between a single-phase cathode (sloped voltage profile) and phase-equilibrium anode (flat voltage profile), the cathode potential (vs. Li/Li^+)

is fixed. Under these conditions, any current passing through the cathode is due to oxidation reactions (comprising the electrolyte, cathode, and/or inactive electrode components: conductive carbon, current collector, coin cell parts).[41] Therefore, measurements of the saturation current (after an initial polarization relaxation) or total charge during a potentiostatic hold can be used to measure electrolyte oxidation and gauge relative electrolyte interfacial stability.[40]

When the electrolyte is in contact with NMC at a voltage higher than its anodic stability limit, electron transfer from the electrolyte to the NMC ensues. These electrons cannot change the oxidation state of the TMs in the NMC, which is dictated by the fixed voltage during the potentiostatic hold. The electrons thus released from electrolyte oxidation travel through the potentiostat to the anode, in this case LTO, participating in lithiation reactions and closing the circuit, giving rise to the measured current. As a result of the NMC state of charge being unchanged by this reaction, the net reaction is given by Eq. 2, in which a number "n" of a generalized electrolyte component "El" is oxidized, resulting in electron transfer to a partially lithiated LTO anode ($Li_{4+a+n}Ti_5O_{12}, a < 3$):

$$nEl + nLiPF_6 + Li_{4+a}Ti_5O_{12} \rightarrow nEl^+ + nPF_6^- + Li_{4+a+n}Ti_5O_{12} \quad (2)$$

Therefore, the saturation currents shown in Figure 4 can be interpreted as the oxidation current during the potentiostatic holds. Consistent with chemical intuition and our DFT results indicating that the fluorinated DFEC and HFDEC are more stable against oxidation, where the FE-3 electrolyte cell shows the lowest oxidation current in the group. For this predicted reaction, consistent with the hydrogen-transfer reaction predicted by the simulations, the generalized El molecule in Eq. 2 could be the EC or EMC component in the Gen2 baseline electrolyte, with El^+ representing the EC*/EMC* and H^+ components of the electrolyte after hydrogen abstraction and subsequent OH group oxidation, leading to an acidified solution..

However, stability against purely electrochemical oxidation is not the only explanation as to the difference between the oxidation currents of the cells containing Gen2 and Gen2+TTFP electrolytes. Our simulations also predicted oxygen abstraction from the cathode surface by the TTFP molecule. Therefore, we have to consider potential contributions of oxygen-anion oxidation to the measured current.

In addition to electrolyte oxidation, the NMC oxygen redox system can also be activated at high voltages.[42] This phenomenon is notably associated with the large irreversible capacities of the lithium manganese rich cathodes and the lithium iron oxide, in which each oxygen oxidation reaction leads to the release of two lithium ions.[43-46] Recent work by Jung et al. shows the effect of both cathode composition and upper cutoff voltage on oxygen loss of various NMC cathodes.[47] In an open circuit conformation, the electrons are transferred from the oxygen to the TM ion, which decreases the average voltage of the lithium metal oxide (Eq. 3).

$$Li_xM_yO_z \rightarrow Li_xM_y\ O_{z-1} + \ O \quad (3)$$

During a potentiostatic hold, however, these electrons are forced to travel to the anode through the external circuit, as was the case for the electrons stemming from electrolyte oxidation described above (Eq. 4).

$$Li_xM_yO_z + Li_{4+a}Ti_5O_{12} \rightarrow Li_{x-2}M_y\ O_{z-1} + Li_{4+a+2}Ti_5O_{12} + O \quad (4)$$

The generated oxygen is unlikely to remain unreacted in the electrolyte, and will chemically oxidize any electrolyte component susceptible to electrophilic attack (Eq. 5).

$$Li_xM_yO_z + Li_{4+a}Ti_5O_{12} + El \rightarrow Li_{x-2}M_y\ O_{z-1} + Li_{4+a+2}Ti_5O_{12} + ElO \quad (5)$$

Therefore, both chemical oxidation (incorporation of atomic oxygen) and electrochemical oxidation (loss of an electron) of the electrolyte will give rise to a measurable oxidation current during a potentiostatic hold. For example, previous research has indicated that TTFP-containing electrolytes, such as our Gen2 + 10% TTFP, will be converted to TTFPa, the phosphate equivalent of the TTFP molecule, during high-voltage holds.[48] For this reaction, the oxygen is thought to originate from the cathode surface. In this case, the general "El" component in Eq. 5 is TTFP, the oxidation product "ElO" is the TTFPa group.

This TTFP reaction provides a viable pathway for oxygen to leave the cathode surface. Therefore, while electrochemical oxidation of the electrolyte simply uses the cathode as a catalytic surface, chemical oxidation of the electrolyte involves the cathode as a reactant. Consequentially, a much larger degree of oxygen loss can be expected from the NMC particles cycled in the Gen2+TTFP electrolyte than in the FE-3 or pure Gen2 electrolytes. This oxygen loss is necessary to form reduced TM environments with a lower M/O atomic ratio, such as spinel M_3O_4 and rock salt MO.[49] This oxygen loss reaction could favorably continue until the rock salt phase is reached, in which M would be in the +2 state and unlikely to undergo further reduction.[47, 50] Transitioning from a $LiMO_2$-type crystal structure to the M_3O_4 and MO crystal structures requires the loss of lithium and oxygen from the cathode surface, and both of these mechanisms are detected. It is important to note, however, that not all spinel regions are indicative of oxygen loss from the structure. M migration in a delithiated, layered Li_xMO_2 structure can change the local crystal structure to spinel $Li_{2x}M_2O_4$; however the M/O ratio is preserved and the M oxidation state is unchanged. While this process would lead to regions with local spinel symmetry in TEM micrographs, no oxygen loss is required (or allowed) for this crystallographic transition. Therefore, observation of spinel areas by TEM characterization alone is not sufficient evidence for oxygen loss. This is likely the case for the sample cycled in FE-3 electrolyte shown in Figure 7c, where O loss is not as likely as in the other two electrolytes.

However, coupled with the electrochemical results, the expectation of oxygen loss and spinel formation is consistent with the STEM and EELS results presented above. The large deviations of ΔE from the bulk value seen in the cathodes cycled in Gen2 and Gen2+TTFP electrolytes point to O loss from the NMC. As previously stated, these changes extend much deeper in the Gen2+TTFP cycled sample than in the Gen2 or FE-3 samples, consistent with TTFP oxidation acting as an oxygen sink. Incorporating the electrochemical consequences of oxygen-anion oxidation, a reaction in which the TTFP removes oxygen from the cathode surface (and subsequently removes lithium from the cathode), is consistent with the high currents and charge passed attributable to oxygen activity observed with the Gen2+TTFP electrolyte (Table 1). This observation also correlates well with the surface reconstruction layers described in Figures 5 and 8. Compared with the TTFP molecules, Gen2 solvent molecules have a lower affinity for oxygen from the cathode. Subsequently, the charge passed during the potentiostatic hold is lower and the O-K pre-peak indicates a higher oxidation state, consistent with less cathode-surface reconstruction. The FE-3 electrolyte shows the smallest reconstructed layer (lowest oxygen loss), the lowest charge passed, and therefore indicates the most stable cathode/electrolyte interface.

Table 1. Average final current and total charge passed during the potentiostatic hold with each of the electrolytes.

	Gen2 + 10%TTFP	Gen2	FE-3
Final average current (μA)	22	0.84	0.46
Total charge passed (mAh)	1.4	0.14	0.09

5. Conclusions

The results presented herein show that the identity of the electrolyte greatly affects the interaction at NMC cathode/electrolyte interfaces and subsequent surface degradation under high-voltage conditions. Additionally, the mechanisms of electrolyte oxidation involved at the charged cathode surface are unique to each electrolyte system and subsequently dictate the extent of cathode-surface degradation through the electrolyte's affinity for both chemical and electrochemical oxidation. Simulation results indicated that for the three electrolyte components that reacted with the NMC surface (TTFP, EC, and EMC), the oxidation mechanism did not involve direct transfer of electrons from the electrolyte to the cathode. Instead, oxidation proceeded through either the conversion of anionic oxygen from the cathode to atomic, yet formally reduced, oxygen in TTFPa (with Gen2+TTFP electrolyte), or, through the transfer of atomic hydrogen from the solvent to the cathode (with Gen2 electrolyte). In the latter case, the newly formed OH group would then oxidize, releasing a proton into the electrolyte and acidifying the solution. These distinct dominant mechanisms would result in two different resultant systems: one with an oxygen depleted, undercoordinated TM surface, and the other with an acidic electrolyte. Understanding the long-term effects of either outcome would be of great interest. The highly fluorinated electrolyte showed very little interaction with the cathode surface revealing little to no electron or hydrogen transfer as well as low oxygen affinity. Correspondingly, this system showed a negligible increase in the thickness of the disordered layer on the cathode surface.

Acknowledgements

We gratefully acknowledge support from the U. S. Department of Energy (DOE), Office of Energy Efficiency and Renewable Energy, Vehicle Technologies Office. Argonne National Laboratory is operated for DOE Office of Science by UChicago Argonne, LLC, under contract number DE-AC02-06CH11357.

We gratefully acknowledge the computing resources provided on Bebop, a high-performance computing cluster operated by the Laboratory Computing Resource Center at Argonne National Laboratory. This research also used resources of the National Energy Research Scientific Computing Center (NERSC), a U.S. Department of

Energy Office of Science User Facility operated under Contract No. DE-AC02-05CH11231.

R. Shahbazian-Yassar and S. Sharifi-Asl acknowledge the financial support from National Science Foundation DMR-1620901

References

[1] Nitta, N., Wu, F., Lee, J.T., Yushin, G. Li-ion battery materials: present and future. Mater. Today. 2015, 18, 252-64.
[2] Dahn, J.R., Fuller, E.W., Obrovac, M., von Sacken, U. Thermal stability of LixCoO2, LixNiO2 and λ-MnO2 and consequences for the safety of Li-ion cells. Solid State Ionics. 1994, 69, 265-70.
[3] Whittingham, M.S. Lithium batteries and cathode materials. Chem. Rev. 2004, 104, 4271-302.
[4] Hausbrand, R., Cherkashinin, G., Ehrenberg, H., Gröting, M., Albe, K., Hess, C., et al. Fundamental degradation mechanisms of layered oxide Li-ion battery cathode materials: Methodology, insights and novel approaches. Materials Science and Engineering: B. 2015, 192, 3-25.
[5] Wang, L., Maxisch, T., Ceder, G. A First-Principles Approach to Studying the Thermal Stability of Oxide Cathode Materials. Chem. Mater. 2007, 19, 543-52.
[6] Armstrong, A.R., Holzapfel, M., Novák, P., Johnson, C.S., Kang, S.-H., Thackeray, M.M., et al. Demonstrating Oxygen Loss and Associated Structural Reorganization in the Lithium Battery Cathode Li[Ni0.2Li0.2Mn0.6]O2. J. Am. Chem. Soc. 2006, 128, 8694-8.
[7] Wang, H., Jang, Y.I., Huang, B., Sadoway, D.R., Chiang, Y.M. TEM Study of Electrochemical Cycling‐Induced Damage and Disorder in LiCoO2 Cathodes for Rechargeable Lithium Batteries. J. Electrochem. Soc. 1999, 146, 473-80.
[8] Zheng, H., Sun, Q., Liu, G., Song, X., Battaglia, V.S. Correlation between dissolution behavior and electrochemical cycling performance for LiNi1/3Co1/3Mn1/3O2-based cells. J. Power Sources. 2012, 207, 134-40.
[9] Egashira, M., Takahashi, H., Okada, S., Yamaki, J.-i. Measurement of the electrochemical oxidation of organic electrolytes used in lithium batteries by microelectrode. J. Power Sources. 2001, 92, 267-71.
[10] Arora, P., White, R.E., Doyle, M. Capacity Fade Mechanisms and Side Reactions in Lithium‐Ion Batteries. J. Electrochem. Soc. 1998, 145, 3647-67.
[11] Kang, K.S., Choi, S., Song, J., Woo, S.-G., Jo, Y.N., Choi, J., et al. Effect of additives on electrochemical performance of lithium nickel cobalt manganese oxide at high temperature. J. Power Sources. 2014, 253, 48-54.

[12] Wang, D.Y., Xia, J., Ma, L., Nelson, K.J., Harlow, J.E., Xiong, D., et al. A Systematic Study of Electrolyte Additives in Li[Ni1/3Mn1/3Co1/3]O2 (NMC)/Graphite Pouch Cells. J. Electrochem. Soc. 2014, 161, A1818-A27.
[13] Zhang, Z., Hu, L., Wu, H., Weng, W., Koh, M., Redfern, P.C., et al. Fluorinated electrolytes for 5 V lithium-ion battery chemistry. Energy & Environmental Science. 2013, 6, 1806-10.
[14] Bolloli, M., Kalhoff, J., Alloin, F., Bresser, D., Phung Le, M.L., Langlois, B., et al. Fluorinated Carbamates as Suitable Solvents for LiTFSI-Based Lithium-Ion Electrolytes: Physicochemical Properties and Electrochemical Characterization. The Journal of Physical Chemistry C. 2015, 119, 22404-14.
[15] He, M., Hu, L., Xue, Z., Su, C.C., Redfern, P., Curtiss, L.A., et al. Fluorinated Electrolytes for 5-V Li-Ion Chemistry: Probing Voltage Stability of Electrolytes with Electrochemical Floating Test. J. Electrochem. Soc. 2015, 162, A1725-A9.
[16] Hu, L., Amine, K., Zhang, Z. Fluorinated electrolytes for 5-V Li-ion chemistry: Dramatic enhancement of LiNi0.5Mn1.5O4/graphite cell performance by a lithium reservoir. Electrochem. Commun. 2014, 44, 34-7.
[17] Hu, L., Zhang, Z., Amine, K. Fluorinated electrolytes for Li-ion battery: An FEC-based electrolyte for high voltage LiNi 0.5 Mn 1.5 O 4/graphite couple. Electrochem. Commun. 2013, 35, 76-9.
[18] Xia, J., Nie, M., Burns, J.C., Xiao, A., Lamanna, W.M., Dahn, J.R. Fluorinated electrolyte for 4.5 V Li(Ni0.4Mn0.4Co0.2)O2/graphite Li-ion cells. J. Power Sources. 2016, 307, 340-50.
[19] Lin, F., Markus, I.M., Nordlund, D., Weng, T.-C., Asta, M.D., Xin, H.L., et al. Surface reconstruction and chemical evolution of stoichiometric layered cathode materials for lithium-ion batteries. Nature Communications. 2014, 5, 3529.
[20] Lin, F., Nordlund, D., Pan, T., Markus, I.M., Weng, T.-C., Xin, H.L., et al. Influence of synthesis conditions on the surface passivation and electrochemical behavior of layered cathode materials. Journal of Materials Chemistry A. 2014, 2, 19833-40.
[21] Jung, S.-K., Gwon, H., Hong, J., Park, K.-Y., Seo, D.-H., Kim, H., et al. Understanding the Degradation Mechanisms of LiNi0.5Co0.2Mn0.3O2 Cathode Material in Lithium Ion Batteries. Advanced Energy Materials. 2014, 4, n/a-n/a.
[22] Steiner, J.D., Mu, L., Walsh, J., Rahman, M.M., Zydlewski, B., Michel, F.M., et al. Accelerated Evolution of Surface Chemistry Determined by Temperature and Cycling History in Nickel-Rich Layered Cathode Materials. ACS Appl. Mater. Interfaces. 2018, 10, 23842-50.
[23] Xu, B., Fell, C.R., Chi, M., Meng, Y.S. Identifying surface structural changes in layered Li-excess nickel manganese oxides in high voltage lithium ion batteries: A joint experimental and theoretical study. Energy & Environmental Science. 2011, 4, 2223-33.
[24] He, M., Su, C.-C., Peebles, C., Feng, Z., Connell, J.G., Liao, C., et al. Mechanistic Insight in the Function of Phosphite Additives for Protection of LiNi0.5Co0.2Mn0.3O2 Cathode in High Voltage Li-Ion Cells. ACS Appl. Mater. Interfaces. 2016, 8, 11450-8.
[25] Tornheim, A., He, M., Su, C.-C., Zhang, Z. The Role of Additives in Improving Performance in High Voltage Lithium-Ion Batteries with Potentiostatic Holds. J. Electrochem. Soc. 2017, 164, A6366-A72.

[26] Kresse, G., Furthmüller, J. Efficiency of ab-initio total energy calculations for metals and semiconductors using a plane-wave basis set. Computational materials science. 1996, 6, 15-50.
[27] Kresse, G., Hafner, J. Ab initio molecular dynamics for liquid metals. Physical Review B. 1993, 47, 558.
[28] Perdew, J.P., Burke, K., Ernzerhof, M. Generalized gradient approximation made simple. Phys. Rev. Lett. 1996, 77, 3865.
[29] Blöchl, P.E. Projector augmented-wave method. Physical review B. 1994, 50, 17953.
[30] Iddir, H., Benedek, R. First-Principles Analysis of Phase Stability in Layered–Layered Composite Cathodes for Lithium-Ion Batteries. Chem. Mater. 2014, 26, 2407-13.
[31] Heyd, J., Scuseria, G.E., Ernzerhof, M. Hybrid functionals based on a screened Coulomb potential. The Journal of Chemical Physics. 2003, 118, 8207-15.
[32] Mathew, K., Hennig, R.G. Implicit self-consistent description of electrolyte in plane-wave density-functional theory. arXiv preprint arXiv:1601.03346. 2016.
[33] Mathew, K., Sundararaman, R., Letchworth-Weaver, K., Arias, T., Hennig, R.G. Implicit solvation model for density-functional study of nanocrystal surfaces and reaction pathways. The Journal of chemical physics. 2014, 140, 084106.
[34] Frisch, M., Trucks, G., Schlegel, H.B., Scuseria, G., Robb, M., Cheeseman, J., et al. Gaussian 09, revision D. 01. Gaussian, Inc., Wallingford CT, 2009.
[35] Garcia, J.C., Bareño, J., Yan, J., Chen, G., Hauser, A., Croy, J.R., et al. Surface Structure, Morphology, and Stability of Li (Ni1/3Mn1/3Co1/3) O2 Cathode Material. The Journal of Physical Chemistry C. 2017, 121, 8290-9.
[36] Ohzuku, T., Ueda, A., Yamamoto, N. Zero‐Strain Insertion Material of Li [Li1 / 3Ti5 / 3] O 4 for Rechargeable Lithium Cells. J. Electrochem. Soc. 1995, 142, 1431-5.
[37] Sharifi-Asl, S., Soto, F.A., Nie, A., Yuan, Y., Asayesh-Ardakani, H., Foroozan, T., et al. Facet-Dependent Thermal Instability in LiCoO2. Nano Lett. 2017, 17, 2165-71.
[38] Zhao, Y., Feltes, T.E., Regalbuto, J.R., Meyer, R.J., Klie, R.F. In situ electron energy loss spectroscopy study of metallic Co and Co oxides. J. Appl. Phys. 2010, 108, 063704.
[39] Karki, K., Huang, Y., Hwang, S., Gamalski, A.D., Whittingham, M.S., Zhou, G., et al. Tuning the Activity of Oxygen in LiNi0.8Co0.15Al0.05O2 Battery Electrodes. ACS Appl. Mater. Interfaces. 2016, 8, 27762-71.
[40] Tornheim, A., Trask, S.E., Zhang, Z. Evaluation of Electrolyte Oxidation Stability on Charged LiNi0. 5Co0. 2Mn0. 3O2 Cathode Surface through Potentiostatic Holds. J. Electrochem. Soc. 2016, 163, A1717-A22.
[41] Smith, A.J., Burns, J.C., Xiong, D., Dahn, J.R. Interpreting High Precision Coulometry Results on Li-ion Cells. J. Electrochem. Soc. 2011, 158, A1136-A42.
[42] Assat, G., Delacourt, C., Corte, D.A.D., Tarascon, J.-M. Editors' Choice—Practical Assessment of Anionic Redox in Li-Rich Layered Oxide Cathodes: A Mixed Blessing for High Energy Li-Ion Batteries. J. Electrochem. Soc. 2016, 163, A2965-A76.

[43] Deng, Z.Q., Manthiram, A. Influence of Cationic Substitutions on the Oxygen Loss and Reversible Capacity of Lithium-Rich Layered Oxide Cathodes. The Journal of Physical Chemistry C. 2011, 115, 7097-103.
[44] Johnson, C.S., Kang, S.H., Vaughey, J.T., Pol, S.V., Balasubramanian, M., Thackeray, M.M. Li2O Removal from Li5FeO4: A Cathode Precursor for Lithium-Ion Batteries. Chem. Mater. 2010, 22, 1263-70.
[45] Rana, J., Stan, M., Kloepsch, R., Li, J., Schumacher, G., Welter, E., et al. Structural Changes in Li2MnO3 Cathode Material for Li-Ion Batteries. Advanced Energy Materials. 2014, 4, 1300998-n/a.
[46] Robertson, A.D., Bruce, P.G. Mechanism of electrochemical activity in Li2MnO3. Chem. Mater. 2003, 15, 1984-92.
[47] Jung, R., Metzger, M., Maglia, F., Stinner, C., Gasteiger, H.A. Chemical versus Electrochemical Electrolyte Oxidation on NMC111, NMC622, NMC811, LNMO, and Conductive Carbon. The Journal of Physical Chemistry Letters. 2017, 4820-5.
[48] Sahore, R., Tornheim, A., Peebles, C., Garcia, J., Dogan, F., O'Hanlon, D.C., et al. Methodology for understanding interactions between electrolyte additives and cathodes: a case of the tris(2,2,2-trifluoroethyl)phosphite additive. Journal of Materials Chemistry A. 2018, 6, 198-211.
[49] Phillips, P.J., Bareño, J., Li, Y., Abraham, D.P., Klie, R.F. On the Localized Nature of the Structural Transformations of Li2MnO3Following Electrochemical Cycling. Advanced Energy Materials. 2015, 5, 1501252.
[50] Jung, R., Metzger, M., Maglia, F., Stinner, C., Gasteiger, H.A. Oxygen Release and Its Effect on the Cycling Stability of LiNixMnyCozO2 (NMC) Cathode Materials for Li-Ion Batteries. J. Electrochem. Soc. 2017, 164, A1361-A77.

Adam Tornheim is a postdoctoral research fellow in the department of Electrochemical Energy Storage at Argonne National Laboratory. He received his PhD degree from University of California, Berkeley in 2013 and B.S. degree from Brandeis University in 2006. His research interests focus on energy storage and electrochemistry, with a specific focus on electrode-electrolyte interactions.

Soroosh Sharifi-Asl is currently a PhD candidate in the Mechanical Engineering department at the University of Illinois at Chicago advised by Dr. Shahbazian-Yassar. He earned his M.S. degree in Materials Science from University of Tehran in 2014. His current research is focused on studying the structural and thermal stability of Li-ion battery cathodes by *in-situ* electron microscopy technique.

Juan Garcia is a postdoctoral appointee in the Chemical Sciences and Engineering Division at Argonne National Laboratory. He is a chemical engineer by training and he received a PhD degree on computational chemistry at Worcester Polytechnic Institute in 2014. His research interest includes multiscale modeling, high performance computing and software development. Before joining Argonne, he worked as a postdoctoral researcher at the Technical University of Eindoven in the Netherlands. In Argonne, he works on the molecular modeling of Li-ion battery materials with the goal of enable high energy and high voltage systems.

Javier Bareño received his Ph.D. in Materials Science from the University of Illinois at Urbana-Champaign. As a Postdoctoral Researcher and, later, a Materials Scientist at Argonne National Laboratory, his research focused on understanding the materials-level processes responsible for performance degradation and failure of Lithium-ion and related batteries. His scientific interests include texture and microstructure development and evolution in thin films and electrode active materials, as well as their influence on macroscopic properties. He is currently Scientific Advisor at MIMSI Materials.

Hakim Iddir is an Assistant Physicist at Argonne National Laboratory (ANL). Dr. Iddir holds a Ph.D. in Physics from the University of Illinois at Chicago, a Master of Chemical Engineering from the Illinois Institute of Technology in Chicago.
His research interests are in the area of materials science, with a focus on developing experimental and theoretical approaches for investigating structure-property relationships at the atomic scale, defects, surfaces, interfaces in materials, chemical and physical properties of catalytic, non-catalytic and energy materials.

Dr. Reza Shahbazian-Yassar is an associate professor of Mechanical Engineering at the University of Illinois at Chicago. Prior to this position, he was an assistant and then associate professor at Michigan Technological University from 2007 to 2015. He received his Ph.D. in Materials Science from Washington State University in Pullman, WA, in Dec 2005. He has published more than 126 journal papers and four book chapters. His research is mainly focused on (1) in-situ TEM of functional nanomaterials; (2) material design and discovery for safe and high energy density batteries; and (3) advanced manufacturing for batteries.

Dr. Zhengcheng (John) Zhang is a Chemist/Group leader of Advanced Electrolyte Research Group at Argonne National Laboratory. Dr. Zhang received his Ph.D. degree in polymer chemistry from Institute of Chemistry, Chinese Academy of Sciences in 2000. He has 20 years of experience in organic material research for electrochemical energy storage systems. His research focuses on the design, synthesis and characterization of new organic materials for next generation Li-ion batteries, Li-S batteries and redox flow batteries. He has won R&D 100 Awards three times and edited one Springer book for rechargeable batteries. He has published 140 papers in peer-reviewed journals, 6 book chapters and holds 50 patents and patent applications.